Date:	Jun 03 2021 02:50AM
To:	"Irene Jiménez-Fortunato" irene.jimenez-fortunato@bristol.ac.uk
cc:	"Daniel J. Bull" daniel.bull@soton.ac.uk;danjonbull@aol.com, "Ole T. Thomsen" o.thomsen@bristol.ac.uk;ott@m-tech.aau.dk, "Janice M. Dulieu-Barton" janice.barton@bristol.ac.uk
From:	"N. Takeda" takeda@smart.k.u-tokyo.ac.jp
Subject:	Your Submission to Composites Part A

Ms. Ref. No.: JCOMA-21-151R2
Title: On the source of the thermoelastic response from orthotropic fibre reinforced composite laminates
Composites Part A

Dear Dr. Irene Jiménez-Fortunato,

I am delighted to say that your paper has been accepted for publication in Composites Part A.

Your accepted manuscript will now be transferred to our production department and work will begin on creation of the proof. If we need any additional information to create the proof, we will let you know. If not, you will be contacted again in the next few days with a request to approve the proof and to complete a number of online forms that are required for publication.

We rely on expert reviews to maintain the high standard of Composites Part A and this has helped improve our impact factor from 3.07 in 2014 to 6.44 in 2019. Last year we received about 3000 manuscripts of which only 13% made it through the review process. All published papers require at least two reviews. We trust that you will continue to support the journal by carrying out your share of these, and if you are not able to help, by suggesting alternative reviewers.

Yours sincerely,

N. Takeda, PhD
Asian Editor Appl. Sci. & Manufacturing
Composites Part A

Editor/referees' comments:

****

EDITORS' CONTACT DETAILS:

Prof. Michael Wisnom
Editor-in-Chief and Editor for Europe and Africa (Applied Science)
Email: Composites-Part-A@bristol.ac.uk

Prof. Kristiina Oksman
Editor for Biocomposites
Email: kristiina.oksman@ltu.se

Prof. Nobuo Takeda
Editor for Asia and Australasia (Applied Science)
Email: Takeda@smart.k.u-tokyo.ac.jp

Prof. Suresh Advani
Editor (Manufacturing) and American Editor (Applied Science and Manufacturing)
Email: advani@me.udel.edu

Prof. Jang-Kyo Kim
Editor for Nanocomposites
Email: mejkkim@ust.hk

Prof. Zhong Zhang
Chinese Editor (Applied Science
Email: coco_zz@nanoctr.cn

On the source of the thermoelastic response from orthotropic fibre reinforced composite laminates

Irene Jiménez-Fortunato[1,2,*], Daniel J. Bull[1], Ole T. Thomsen[2], Janice M. Dulieu-Barton[2]

[1]School of Engineering, University of Southampton, UK

[2]Bristol Composites Institute (ACCIS), University of Bristol, UK

*Corresponding author: irene.jimenez-fortunato@bristol.ac.uk

Abstract

In thermoelastic stress analysis (TSA) of orthotropic laminated polymer composites, heat transfer influences the measured stress induced temperature change, or 'thermoelastic response'. The composite constituents, including different fibre types, fibre geometry, ply thickness and resin systems, in combination with the manufacturing process means that, even for nominally identical materials, different conditions are generated for heat transfer. Hence, definitively identifying the 'source' of the thermoelastic response for a general composite laminate has remained elusive. A procedure based on the simultaneous application of digital image correlation (DIC) and TSA is devised that enables the source of the thermoelastic response to be established categorically. In glass fibre laminates, it is shown that heat conduction cannot take place so the thermoelastic response emanates from the surface resin rich layer. In similar carbon fibre laminates, adiabatic conditions are only met at higher frequencies with the response emanating from the orthotropic surface ply.

Keywords: B-Thermomechanical, B-Optical properties/techniques, D-Thermal analysis, D-Mechanical testing

1. Introduction

Thermoelastic stress analysis (TSA) [1] is a well-established full-field non-contact technique that depends on the thermoelastic effect, which is the reversible relationship between thermal energy and mechanical deformation under adiabatic conditions. A sinusoidal cyclic load is required so that the peak-to-peak temperature change, ΔT, or thermoelastic response, can be extracted from a temperature signal measured with an infrared (IR) detector. Over the past three decades, TSA has been successfully applied in a wide range of engineering applications. In 1988 [2], the relationship between ΔT and the stresses in an orthotropic composite material was first established as:

$$\Delta T = -\frac{T_0}{\rho C_p}(\alpha_1 \Delta\sigma_1 + \alpha_2 \Delta\sigma_2 + \alpha_6 \Delta\sigma_6) \quad (1)$$

where T_0 is the mean surface temperature, ρ is the density of the material, C_p is the specific heat capacity at constant pressure, α is the coefficient of linear thermal expansion, $\Delta\sigma$ is the change in stress and the subscripts are given in standard contracted tensor notation for a plane orthotropic body relative to the principal material directions [3].

Equation (1) provides the thermoelastic response from a general orthotropic body, which does not incorporate the features from an actual laminated composite structure. It is valid only when ΔT occurs adiabatically, but as pointed out in [4] ΔT changes ply-by-ply and drives heat transfer. Over the decades since the publication of [4], there have been many publications, e.g. [5-14], attempting to interpret the thermoelastic response from laminated polymer composite materials. Zhang et al. [5] studied unidirectional (UD) carbon/epoxy composites and determined that the thermoelastic response became independent of the surface ply for resin-rich surface layers in excess of 30 μm in thickness. Cunningham et al. [6] came to a similar conclusion for E-glass/epoxy pre-preg material. Pitarresi et al. [7] studied glass/polyester composites and showed that the resin-rich layer acted as an isotropic ‘strain witness’ (i.e. thermally isolated from the laminate stack so the response is generated by the strain experienced by the resin layer) reproducing the strain field of the laminate underneath, which was later confirmed in [8] using analytical models. Emery et al. [9] determined that in an oven consolidated glass/epoxy laminate the 25 μm thick resin-rich layer was sufficient to provide a strain witness, and developed thermoelastic relationships for ply lay-ups in terms of strain. Sambasivam et al. [10] used classical laminate theory (CLT) to derive the

thermoelastic response from the surface ply, resin-rich layer, or multidirectional composite laminate, but the outcome was largely inconclusive because of the need to estimate various material properties. In summary, the above works highlight the important influence of the resin-rich surface layer on the thermoelastic response.

Fruehmann et al. [11] showed that variations in fibre volume fraction have significant influence on the thermoelastic response from polymer composite materials, and likewise in [12] demonstrated the sensitivity to variations on the fibre volume fraction, resin material and manufacturing methods of glass/epoxy composites. Only one publication [7] thus far has considered the paint coating that is used in TSA to create a uniform and enhanced surface emissivity. It was seen that at low loading frequencies the paint layer acts as an amplifier of the thermoelastic response from the sample, but at high loading frequencies, it acts as a strain witness; similar observations were made in [13] where pure epoxy resin was studied. These effects are attributed to non-adiabatic behaviour, where at higher loading frequencies the thermal diffusion length is small, so the heat cannot diffuse through the paint, and for thicker coating the paint acts as a strain witness and attenuates the thermoelastic response. In [14], laminated carbon fibre epoxy specimens with different stacking sequences were studied. The stacking sequence had a marked effect on the thermoelastic response with some lay-ups showing an increase in response with frequency and others a decrease.

It is clear from the above that ΔT is influenced by the construction of the laminate and its constituent materials. Furthermore, the thickness of the resin-rich layer on the surface of the laminate influences the response, as well as the ply thickness and the fibre volume fraction. The thickness of the resin-rich layer is controlled by the manufacturing process and generally comprises a very low conductivity polymer. The heat transfer between the plies is driven by the thermal conductivity and diffusivity of the constituent materials. The ply-by-ply stresses, and hence, ΔT in each ply, are controlled by the laminate material and fibre orientations, and the relative direction and magnitude of the global applied strain. If ΔT is large, then this may be sufficient to drive substantial heat conduction into the surface layer. The loading frequency controls the heat transfer; as the loading frequency increases, the thermal diffusion length decreases and, depending on the material conductivity, the temperature change occurs under adiabatic conditions. The great number of variables that play a role in the thermoelastic response from laminated orthotropic

composites motivates further investigation if the technique is to be applied to structural components with an aim to provide quantitative information about the material stress state.

The purpose of the work described in the present paper is to understand the nature of the thermoelastic response by introducing an independent measure of the in-plane strains without any influence of heat transfer using the digital image correlation (DIC) technique [15]. In DIC, a speckle pattern applied to the surface of the sample is tracked while the sample is deforming. For sinusoidal loading conditions, it is possible to obtain the change in strain, $\Delta\varepsilon$, from DIC by using the same algorithm as for TSA [16]. In this work, the process used is based on the least-squares algorithm, and the methodology is referred to as 'Least-Squares DIC' (LSDIC). The strains derived from the LSDIC are validated against strain gauge readings, and it is demonstrated that TSA can be conducted with LSDIC to provide full-field data relating to both the stress (TSA) and strain (DIC) fields. The application of LSDIC alongside TSA not only removes the need to have a priori knowledge of many mechanical properties, but also any inconsistencies in the loading by eliminating the need to calculate the stresses from the applied load.

Strips of multidirectional symmetrically laminated composite material loaded in tension are studied. Assuming there is no damage in the material in its virgin as manufactured state, the DIC measure of surface strain allows the global (overall laminate) and the ply-by-ply stresses to be determined using only the measured elastic constants. Section 2 of the paper describes the three different scenarios that are considered for the source of the thermoelastic response: 1) the stresses in resin-rich surface layer, 2) the stresses in the orthotropic surface ply and 3) the global laminate mechanical response. The nomenclature is explained diagrammatically in Figure 1.

Both low conductivity Glass Fibre Reinforced Polymer (GFRP) and high conductivity Carbon Fibre Reinforced Polymer (CFRP) are studied, manufactured from two well characterised composite material systems, RP-528 [17] and IM7/8552 [18, 19], respectively. A detailed survey of the literature alongside a comprehensive mechanical testing campaign provides the relevant material properties to calculate ΔT from the DIC strains for the three scenarios. Factors such as paint coating, resin-rich layer thickness and fibre volume fraction are considered. Importantly, the effect of surface emissivity of the material is included in the approach facilitated by measurements against a blackbody source. A significant amount of experimental data has been generated to provide the results described through the paper. All data supporting this study

are openly available from the University of Southampton repository at https://doi.org/10.5258/SOTON/D1828.

The work presents a new procedure for calibration of TSA for use on orthotropic laminated polymer composites. It is demonstrated that such a calibration procedure is necessary to interpret the thermoelastic response from complex structural composites in any quantitative manner. Furthermore, the research presented brings together, for the first time, a means of assessing the significance and influence of many variables that thus far have been considered to be a barrier to deploying TSA in studies of the performance of composite materials and structures.

2. Derivation of Thermoelastic Response from Measured Strains

To establish the effect of heat transfer on the thermoelastic response, it is proposed that a comparison between the measured ΔT obtained from TSA is made with a calculated value determined from the measured strains obtained with LSDIC. The latter is independent of any heat transfer effects, and therefore provides the basis for establishing the effect of different materials and stacking sequences on the thermoelastic response. The theoretical considerations are based on a multidirectional laminated coupon type specimen with a symmetrical stacking sequence loaded in uniaxial tension; the coordinate systems and notation used throughout the paper follows [3] and is shown in Figure 2. The laminate/coupon axes and the principal material directions are denoted in Figure 2 with the load (N_x) applied in the coupon x-direction.

Using the nomenclature shown in Figure 2 and by assuming that strain compatibility is retained through the laminate stack, it is possible to calculate ΔT from the measured laminate strains for three different scenarios as follows:

1) Resin-rich surface layer

The resin-rich surface layer is an isotropic material, so ΔT in the resin, ΔT_r, is related to the stress change in the resin, $\Delta(\sigma_x + \sigma_y)_r$, by the following expression:

$$\Delta T_r = -\frac{eT_0\alpha_r}{\rho_r C_{p_r}}\Delta(\sigma_x + \sigma_y)_r \tag{2}$$

where e is the emissivity of the specimen surface, α_r is the coefficient of thermal expansion of the resin, ρ_r is the density of the resin, and C_{p_r} is the specific heat capacity of the resin at constant pressure.

It is important to note that the term $\Delta(\sigma_x + \sigma_y)_r$ in equation (2) is an invariant, and therefore independent of direction. In the set-up shown in Figure 2, the $x - y$ axes are coincident with the axes of principal stress in the laminate and hence the change in the shear stress, $\Delta\sigma_{xy}$, is neglected (zero) in equation (2), but the term is retained in the following treatment. By obtaining the laminate strain, $[\Delta\varepsilon]_{x,y}$, from the LSDIC, $\Delta\sigma_{x_r}$ and $\Delta\sigma_{y_r}$ are calculated as follow:

$$\begin{bmatrix} \Delta\sigma_x \\ \Delta\sigma_y \\ \Delta\sigma_{xy} \end{bmatrix}_r = [Q]_r \begin{bmatrix} \Delta\varepsilon_x \\ \Delta\varepsilon_y \\ \Delta\varepsilon_{xy} \end{bmatrix} = \begin{bmatrix} \frac{E_r}{1-\nu_r^2} & \frac{\nu_r E_r}{1-\nu_r^2} & 0 \\ \frac{\nu_r E_r}{1-\nu_r^2} & \frac{E_r}{1-\nu_r^2} & 0 \\ 0 & 0 & G_r \end{bmatrix} \begin{bmatrix} \Delta\varepsilon_x \\ \Delta\varepsilon_y \\ \Delta\varepsilon_{xy} \end{bmatrix} \tag{3}$$

where E_r is the Young's modulus of the resin, ν_r is the Poisson's ratio of the resin and G_r is the shear modulus, which is calculated directly from E_r and ν_r as the resin is assumed to be isotropic.

From equations (2) and (3) above, the 'normalised' thermoelastic response can be calculated as

$$\frac{\Delta T_r}{T_0} = -\frac{e\alpha_r}{\rho_r C_{p_r}} \left[\frac{E_r}{1-\nu_r} (\Delta\varepsilon_x + \Delta\varepsilon_y) + G_r \Delta\varepsilon_{xy} \right] \tag{4}$$

In equation (4) the normalising factor, T_0, is the mean of the cyclic temperature change and is obtained from the least-squares processing of the IR images series captured for the TSA. Normalising the thermoelastic response in this manner removes the effect of any variations in specimen temperature during the experiments. It is clear from equation (4) that to calculate the thermoelastic response from measured strains, the elastic constants, density, specific heat capacity and coefficient of thermal expansion are required alongside the emissivity of the surface. The coupon is loaded so that the $x - y$ axes are axes of principal stress and strain (shear strain is zero). However, it is important to note the normal stress/strain sum is an invariant, so issues such as misalignments in the coupon and its clamping can be neglected and, as the resin is isotropic, the coefficient of thermal expansion can be expressed as a scalar quantity.

In the treatment above, it is assumed that the resin-rich surface layer is thermally isolated from the laminate stack and the response is generated by the strain experienced by the resin layer, hence the terminology

'strain witness'. Clearly this is dependent on the magnitude of ΔT in the layer below, if ΔT in the substrate is greater than that in the resin layer then heat will be transferred to the resin layer and vice versa. However, if the thermal conductivity of the resin and the substrate layer is low, then heat transfer between the two can be considered to be negligible, thus creating the so-called strain witness reported in [6-9]. Additionally, the thickness of the resin layer and the substrate layers play a role in the thermal diffusion conditions, indicating a minimum thickness of resin for the strain witness assumption to be valid.

2) Orthotropic surface ply

As with scenario 1, the surface ply is treated as an isolated ply and any heat transfer effects are neglected. Although, it should be noted that some heat transfer may take place, dependent on the loading frequency, constituent materials, the ply thickness, the fibre volume fraction and the fibre orientation relative to the subsurface ply. The nomenclature given in Figure 2 is used, and the directional elastic properties and coefficients of thermal expansion are considered. Here the thermoelastic response is calculated as a function of the properties in the principal material direction of the surface ply, i.e. $\alpha_6 = 0$. Hence, using the measured strains from the LSDIC, the normalised thermoelastic response for the surface ply can be determined as

$$\frac{\Delta T_{surface\ ply}}{T_0} = -\frac{e}{\rho C_p}[\alpha_1 \quad \alpha_2 \quad 0]\begin{bmatrix} \frac{E_1}{1-\nu_{12}\nu_{21}} & \frac{\nu_{21}E_1}{1-\nu_{12}\nu_{21}} & 0 \\ \frac{\nu_{21}E_1}{1-\nu_{12}\nu_{21}} & \frac{E_2}{1-\nu_{12}\nu_{21}} & 0 \\ 0 & 0 & G_{12} \end{bmatrix}[T_e]\begin{bmatrix} \Delta\varepsilon_x \\ \Delta\varepsilon_y \\ \Delta\varepsilon_{xy} \end{bmatrix} \tag{5}$$

where $[T_e]$ is the transformation matrix of the strains from 1-2 in the principal material directions (1 longitudinal and 2 transverse to fibre direction) to the global coordinate system x and y (longitudinal and transverse) as shown in Figure 2, E_1, E_2, ν_{12}, ν_{21} and G_{12} are the elastic coefficients of the orthotropic surface ply, C_p is the specific heat capacity, α_1 and α_2 are the coefficients of thermal expansion longitudinal and transverse to the fibre direction respectively, and $[\Delta\varepsilon]_{x,y}$ is the LSDIC measured change in strain.

Unlike scenario 1, the term G_{12} in equation (5) is independent of the other elastic properties, however, it is coupled with $\alpha_6 = 0$. Moreover, in the loading configuration shown in Figure 2 the laminate axes are axes of principal strain and hence $\Delta\varepsilon_{xy}$ is zero. Nevertheless, the elastic properties longitudinal and transverse to the fibre direction are required to determine the normalised thermoelastic response.

3) Global laminate

In contrast to scenario 1 and 2, here the response is considered to be generated by the homogenised laminate and, hence, all quantities are referenced to the laminate axes shown in Figure 2:

$$\frac{\Delta T_{laminate}}{T_0} = -\frac{e}{\rho C_p}[\alpha_x \quad \alpha_y \quad \alpha_{xy}][A^*]\begin{bmatrix}\Delta\varepsilon_x\\ \Delta\varepsilon_y\\ \Delta\varepsilon_{xy}\end{bmatrix} \tag{6}$$

where $[A^*]$ is the in-plane stiffness matrix of the laminate normalised by the laminate thickness, h, i.e. $[A^*] = \frac{1}{h}[A]$ [3], $[\alpha]_{x,y}$ the matrix of global coefficients of thermal expansion of the laminate [20], and $[\Delta\varepsilon]_{x,y}$ is the measured change in strain from the LSDIC.

The in-plane coefficients of thermal expansion are calculated as follows [20]:

$$[\alpha]_{x,y} = [a]\left[\sum_{k=1}^{n}(z_k - z_{k-1})\left([T_e]^{-1}\begin{bmatrix}\frac{E_1}{1-\nu_{12}\nu_{21}} & \frac{\nu_{21}E_1}{1-\nu_{12}\nu_{21}} & 0\\ \frac{\nu_{21}E_1}{1-\nu_{12}\nu_{21}} & \frac{E_2}{1-\nu_{12}\nu_{21}} & 0\\ 0 & 0 & G_{12}\end{bmatrix}\begin{bmatrix}\alpha_1\\ \alpha_2\\ 0\end{bmatrix}\right)_k\right] \tag{7}$$

where $[a]$ is the in-plane compliance matrix of the laminate [3], k is the designated ply, z is the coordinate of ply k or $k-1$ [20], and n is the total number of plies that form the laminate.

In scenario 3, the properties $[A^*]$ and $[\alpha]_{x,y}$ includes the thickness and stiffness contributions of each ply, and in the present work includes also the thickness and stiffness of the resin-rich surface layer.

The methodology presented above shows the parameters that are required to obtain the normalised thermoelastic response from measured strain data for the three scenarios. Obtaining the thermoelastic response from measured strain data eliminates any variations due to the loading, as the strains obtained from the LSDIC and ΔT derived from the TSA are generated by the same load if the DIC and TSA are performed by the same cyclic loading test. Equations (4), (5) and (6) contain all the parameters that are required to determine ΔT from the measured strain. The next section of the paper details how each of the parameters was obtained so that ΔT calculated from the LSDIC, ΔT_{LSDIC}, can be compared with ΔT derived from the TSA to identify the effect of heat transfer for different materials and stacking sequences.

3. Test Specimens and Material Properties

3.1. Test Specimen Manufacture and Geometry

All the test specimens were manufactured from either GFRP (RP-528 pre-preg [17]) or CFRP (IM7/8552 pre-preg [18, 19]). Panels of the material were manufactured in an autoclave following the manufacturer recommended curing cycles. All panels were made so that peel ply was employed only on the vacuum bag side of the panels, hence each side of the panels has either a 'smooth' surface, which was in contact with the aluminium mould, or a rough surface containing the characteristic peel ply imprint. Strips of material were cut from the panels to make the specimens, to which end tabs were bonded with epoxy resin.

UD specimens, $[0]_{10}$ and $[90]_{10}$, were made for the mechanical testing. For the TSA and LSDIC, test coupons of stacking sequences $[0,90]_{3s}$, $[90,0]_{3s}$ and $[\pm 45]_{3s}$ were prepared. An overview of the final test specimen dimensions is given in Table 1. The stacking sequences were chosen because the two cross-ply laminates have the same stiffness, with different ply-by-ply stresses and thermoelastic constant of the surface ply, and displaying no shearing coupling, hence, little or no heating. For $[\pm 45]_{3s}$, the ply-by-ply stresses are identical and in theory the plies are in thermal equilibrium with no opportunity for heat transfer, although the shearing may cause some heating at higher loading frequencies.

3.2. Elastic Properties

The elastic properties of the GFRP and CFRP materials were determined in tensile tests on UD and $[\pm 45]_{3s}$ specimens according to ASTM D3039 or ASTM D3518. The GFRP specimens were loaded in an Instron 8800 servo-hydraulic test machine fitted with a 100 kN load cell. The CFRP specimens were tested in an Instron ElectroPuls E10000 electrodynamic test machine fitted with a 10 kN load cell. As the specimens were not tested to failure, several repeat tests were carried out on the same specimen at a strain rate of 2 mm/min. The strains were determined by using stereo DIC on one side of the specimen and a T strain gauge rosette (CEA-13-125UT-350) on the other. A comparison of the strains obtained from the DIC and the strain gauges is shown in Figure 3. The plot is for the $[0]_{10}$ sample, and shows good agreement in the strains measured by the two techniques; similar agreement was obtained for the $[90]_{10}$ and $[\pm 45]_{3s}$specimens. The specimens were loaded and unloaded and, as shown in Figure 3 for the $[0]_{10}$ specimen, the sample

behaved elastically with no sign of permanent set or damage; again similar results were obtained for the $[90]_{10}$and $[\pm 45]_{3s}$ samples. The density of the TSA and DIC coupons ($[0,90]_{3s}$, $[90,0]_{3s}$ and $[\pm 45]_{3s}$) was also evaluated by using the specimen measurements given in Table 1 and the mass of the specimens. A summary of the elastic properties and density for both materials is given in Table 2. The parameters for the DIC are provided in Table 12 in the appendix for GFRP and CFRP experiments. The DIC results differ slightly from those of the strain gauges possibly resulting from a small misalignment in the loading causing a slight out-of-plane bending and for this reason, the mean value between DIC and strain gauges was used. Great care was taken to align the strain gauge rosette exactly with the principal material directions; hence only small misalignments would be possible, with negligible effect on the measured strain. G_{12} is included as it is required to calculate the overall laminate stiffness.

The orthotropic elastic properties were obtained experimentally for both GFRP and CFRP materials. However, to calculate the normalised thermoelastic response for the different scenarios, the resin, the thermal properties of GFRP and CFRP, as well as the surface emissivity are also required. The determination of these properties is discussed in sections 3.3, 3.4 and 3.5.

Sambasivam et al. [10] obtained the elastic properties for the actual resin used in the prepreg and showed that there was little difference in the elastic properties quoted from the literature for a 'pure epoxy' and the measured values. Hence, rather than procure the actual resin used in the prepreg and conduct a testing campaign, it was considered to be acceptable to use properties taken from the literature [3, 11] for a pure epoxy, these are given in Table 3.

3.3. Specimen Volume Fraction and Resin Layer Thickness

The specific heat and coefficient of thermal expansion of composite material are difficult to measure in a standard laboratory environment and literature values show a large variation. This is because both properties are dependent on the fibre volume fraction, V_f, which is determined by the constituent materials and the curing process. Hence, a sensible starting point to determine the thermal properties is to obtain the V_f for the cured materials. The thickness of the resin-rich surface layer and the paint also play a role in the heat transfer and, therefore, have an effect on the measured ΔT, hence, it is essential to measure these to properly compare ΔT with ΔT_{LSDIC}.

The V_f and the thickness of the resin-rich surface layer were determined using micrographs of both the GFRP and CFRP $[0,90]_{3s}$, $[90,0]_{3s}$ and $[\pm 45]_{3s}$ materials. The fibre diameter was measured to calculate the V_f by considering the number of fibres contained in the micrograph area. As the DIC and the TSA were performed on the smooth side of the laminates, the resin-rich surface layer thickness was obtained at the smooth side. Additional experiments were performed on painted smooth and peel ply sides of GFRP specimens to analyse the effect of the surface finish and the paint on thermoelastic response measurements. Therefore, the thicknesses of the resin-rich surface layer and the paint were measured on GFRP specimens. A summary of the V_f, resin and paint thicknesses is presented in Table 4. It can be seen that V_f is lower for the GFRP compared with the CFRP and that the resin-rich layer thickness is almost double for the case of the GFRP in comparison with the CFRP. The higher V_f, and thinner resin-rich surface layer in the CFRP can be attributed to differences in the curing cycles for both material systems, in particular, the higher pressure applied to CFRP panels (i.e., 7 bar versus 4 bar for the GFRP). It should be considered that the carbon fibres are much thinner resulting in better compaction, than can be achieved with the thicker glass fibres (see Table 4). Additionally, for the GFRP results, the resin-rich layer and paint is almost doubled on the peel ply side compared with the smooth side. Figure 4 shows that the paint seems to fill the texture on the peel ply side and to add the same thickness layer as on the smooth side. It should be noted that using micrographs to obtain the fibre volume fraction considers only fibre distribution within the ply. In contrast, the burn off and acid digestion techniques to assess fibre volume fraction would account for any resin rich areas in the ply interfaces. As these were small for the laminates investigated, it was considered that the fibre volume fractions obtained from the micrographs were sufficient for the purposes of the present study.

3.4. Thermal Properties

As described in the previous section, it was not possible to measure with any accuracy the thermal properties of the material. Instead, it was decided to compare literature values with those determined from the rule of mixtures for C_p and Schapery's equations for the coefficients of thermal expansion [3], using V_f. The starting point for applying these approaches are the values for the constituent materials, which are given in Table 5 for E-glass fibre and epoxy resin.

The C_p was determined in [9] and [10] as 882 J kg^{-1}K^{-1} and 843 J kg^{-1}K^{-1} respectively. As V_f was given in [9] and [10], these values can be verified against the rule of mixtures [3]. Figure 5 (a) shows C_p plotted against V_f with the values obtained from [9] and [10] indicated in the plot. It is clear that the value from [10] is incorrect or the constituent materials are different, particularly the resin. However, the value from Emery [9] matches closely the expected results, and provides some confidence in the properties given for the constituent material. Hence, C_p provided by the rule of mixtures for $V_f = 0.54 \pm 0.06$ was used for the calculation of $\Delta T/T_0$ for the orthotropic surface ply and global laminate scenarios as is indicated in Figure 5 (a) with a *.

In a similar way to calculating C_p, the V_f and properties of the constituent materials given in Table 5 were used to obtain α_1 and α_2 for the GFRP using Schapery's equations [3] and plotted in Figure 5 (b). Values were taken from the literature, [3], [9] and [10], and plotted in Figure 5 (b). The value chosen for $\alpha_1 = 7 \cdot 10^{-6}$ K^{-1} is from [3] as it matches the Schapery's equation for α_1. It is important to note that for α_1 the value from [9] also corresponds with the Schapery's equation, with the value from [10] once again not corresponding with the theoretical value. In the case of α_2, there is considerable scatter in the literature values with the value from [10] being close to the theoretical prediction. Hence, it was decided to use an average value from [3], [9] and [10], i.e. $\alpha_2 = 30.7 \cdot 10^{-6}$ K^{-1}, as in general, rule of mixtures type formulations are less reliable transverse to the fibre direction [3].

Regarding the CFRP, as the fibre IM7 is anisotropic [3], it is not straightforward to apply the rule of mixtures or use Schapery's equation to determine the coefficients of thermal expansion of the ply [21]. Additionally, there are no reliable properties for the 8552 epoxy resin published in open literature. Therefore, as IM7/8552 is a very well characterised material, the thermal properties were taken from the literature [22-24] as $C_p = 857$ J kg^{-1}K^{-1} [22] and the coefficients of thermal expansion were taken as the mean of the values found in [23] and [24] shown in Table 6, i.e. $\alpha_1 = -0.3 \cdot 10^{-6}$ K^{-1} and $\alpha_2 = 28.4 \cdot 10^{-6}$ K^{-1}, as the V_f are close to the measured $V_f = 0.63 \pm 0.03$.

The ratio of α_2/α_1 can also be verified experimentally performing TSA on UD samples, with the load applied in the x and y directions (see Figure 2). This allows the thermoelastic constants, K_1 and K_2, to be obtained as follows [14]:

$$K_1 = \frac{\alpha_1}{\rho C_p} = \frac{\Delta T}{T_0 \Delta \sigma_x} \text{ and } K_2 = \frac{\alpha_2}{\rho C_p} = \frac{\Delta T}{T_0 \Delta \sigma_y} \quad (8)$$

where ΔT and T_0 are obtained experimentally, and $\Delta\sigma_x$ and $\Delta\sigma_y$ are the applied stresses.

Hence, the ratio of K_2/K_1 can be determined experimentally and compared with α_2/α_1 obtained from the literature. Table 7 shows that the experimental and theoretical values for both GFRP and CFRP are in close correspondence further verifying the values of coefficients of thermal expansion used in the analysis.

3.5. Surface Emissivity

In the literature, the emissivity of a glass fibre epoxy material ranges from 0.79 [9] to 0.95 [25]. Therefore, assuming a value for the emissivity can have a significant effect on the calculated thermoelastic response. To make an estimation of the emissivity of the GFRP material, an experiment was conducted using a temperature controlled blackbody (Infrared Systems Development Corporation, IR-2106/301[1]) with a known emissivity of 0.96 ± 0.02. Two GFRP coupons were placed in front of the blackbody with the smooth side at the front, one without any background paint applied and the other prepared with a matt black background paint with white speckles, as used for the capture of images for the DIC and TSA. Figure 6 shows an IR image of the specimens attached to the blackbody, collected with a Telops FAST M2K[2] photon detector camera. The blackbody and the coupons had a thermocouple attached to their surface to verify they were all at the same temperature. The temperature of the blackbody was adjusted until it was at the same temperature as the specimens of 24 °C. The scene was recorded at 383 Hz frame rate and 1000 image frames were collected and averaged to reduce the temporal noise. The emissivity, e, of GFRP epoxy resin and matt black paint, MBP Electrolube[3], were determined from the following relationship:

$$\frac{\mathrm{DL_S}}{\mathrm{DL_{BB}}} = \frac{e_\mathrm{S}}{e_\mathrm{BB}} \quad (9)$$

where the subscript S refers to GFRP epoxy or paint, BB to blackbody, and DL is digital level measured with the IR camera.

[1] Infrared Systems Development Corporation. IR-2106/301 Blackbody System. https://www.infraredsystems.com/Products/blackbody2106.html

[2] Telops. High-Speed IR Cameras: MWIR. https://www.telops.com/products/high-speed-cameras/mwir-cameras

[3] Electrolube. MBP400 Matt Black Paint. https://electrolube.com/product/mbpmatt-black-paint/#:~:text=Product%20Description,oils%20and%20other%20environmental%20elements

The $DL_{GFRP\ epoxy}$ and DL_{paint} were obtained by averaging an area shown on Figure 6 of 120 x 40 pixels for each sample, and DL_{BB} was obtained by averaging a 120 x 123 pixel area, also indicated on Figure 6. A summary of the digital levels and emissivity can be seen in Table 8. The GFRP epoxy resin and paint have a similar emissivity. To verify the results further, another experiment was conducted with the coupon positions interchanged, which yielded an identical result. As the CFRP was painted, the emissivity for the paint could be used for the experiments on the CFRP.

4. Thermoelastic Response

4.1. Experimental Arrangements

In the previous section, all the material properties for the laminated composite materials, resin and surface properties were established, so that the normalised thermoelastic response for the different scenarios as presented in section 2 can be calculated from the strains obtained from the DIC. For convenience, a summary of all the material properties used in the analysis is given in tabular format in the Appendix.

To make the comparison between the TSA and the DIC by applying the equations in section 2, it is important that the applied loads do not damage the specimens. Therefore, the applied tension loads for the experiments were determined by establishing the first ply failure (FPF) stress for the multidirectional laminated coupons. The FPF was established using the material properties given in [17, 26] and [23, 27] for the GFRP and CFRP respectively using Puck and LarC03 [28] criteria. Table 9 shows the FPF stress and the applied cyclic load and maximum applied stress used in the experiments. To determine the effect of any heat transfer, the tests were carried out at different loading frequencies from 3.1 to 30.1 Hz. It should be noted that the tests on the GFRP were carried out at about 50% of the FPF stress, whereas in the CFRP the test were carried out at about 30%. This was because the test machine was not able to achieve the target load range accurately at higher frequencies.

The GFRP coupons were painted with MBP Electrolube matt black background paint to increase the emissivity for TSA, and white speckles were applied to dehomogenise the surface for DIC. The CFRP coupons were painted with a very thin layer of black matt paint to reduce reflections on the smooth side due to the surface finish. To understand the effect of the painting, TSA was performed on unpainted GFRP

coupons; this was not possible with the CFRP due to a high level of interference due to reflection. Additionally, GFRP specimens were used to compare the effect of the peel ply imprint by performing TSA and DIC on both sides of the samples. For the GFRP specimens an Instron 8800 servo-hydraulic test machine was used to apply the cyclic load and the CFRP specimens were loaded using an Instron ElectroPuls E10000 electrodynamic test machine.

Figure 7 shows a schematic with the position of the IR and white light cameras used for capturing the images for the TSA and stereo DIC. The DIC equipment was setup according to the iDICs guide [29]. It was not necessary to synchronise the IR and white light image capture. Instead, the lock-in approach used to process the IR images was also used on the strains derived from the DIC [16]. The cameras used for the LSDIC were E-lite 5M by LaVision, where a camera frame rate of 1.5 Hz was used, which is below the loading frequencies studied. Hence, the data is undersampled but, as the frame rate and the loading frequency are known, it is possible to reconstruct the signal and obtain the peak-to-peak amplitude using the least-squares algorithm [30]. The DIC performance characteristics are provided in Table 12 in the Appendix. It should be noted that the noise content is different for the GFRP and CFRP experiments because of adjustments in the illumination of the specimens.

As mentioned previously, the IR camera was a Telops FAST M2K, which is capable of capturing at very high frame rates e.g. ~1,000 frames per second. However, it was decided to limit the number of images captured for TSA, and hence a frame rate of 383 Hz was used for the IR camera to minimise aliasing effects, which has been demonstrated to be sufficient, e.g. [31, 32]. So, the IR camera collected 2,000 frames over 5 seconds immediately after the LSDIC images were collected. To verify the LSDIC strain measurements, a T strain gauge rosette (CEA-13-125UT-350) was mounted on the peel ply side of the coupons. The data extracted from the strain gauges was sampled at 500 Hz.

The normalised thermoelastic response was obtained using equations (4), (5) and (6) for the resin-rich surface layer, orthotropic surface ply and global laminate approaches, respectively. The strain changes, $\Delta\varepsilon_x$ and $\Delta\varepsilon_y$ were obtained from the DIC and strain gauges using the least-squares 'lock-in' algorithm on the measured strains.

4.2. Comparing Measured and CLT Predicted Strains

The aim of this section is to validate the LSDIC measured strains by comparing them with the strains obtained with the strain gauges. The advantage of using LSDIC with respect to strain gauges is that it provides a full-field measurement that allows the detection of strain gradients. Therefore, LSDIC would be suitable for testing of structural components. Additionally, the measured strains from LSDIC and strain gauges were compared with the predicted strains at the laminate mid-plane using CLT.

Figure 8 shows the comparison of longitudinal, $\Delta\varepsilon_x$, and transverse, $\Delta\varepsilon_y$, strains for the three GFRP laminates considered. Generally, the LSDIC and strain gauges measured strains show good agreement, which validates the LSDIC technique. However, at the highest frequency, in some cases there is a mismatch between the strain gauge and LSDIC measurements, probably caused by errors in the fitting of the undersampled LSDIC data. The most important observation, most prominently observed in the $\Delta\varepsilon_x$ values for the $[0,90]_{3s}$ and $[90,0]_{3s}$ laminates, is the reduction in strain with frequency. This is caused by the inability of the test machine to maintain a constant load range at higher loading frequencies, justifying the need to make strain measurements rather than rely on outputs from the test machine. It was confirmed by an analysis of the test machine data that the displacement range was reducing with loading frequency even though control features such as 'amplitude control' were initiated. In the $\Delta\varepsilon_y$ values obtained for the $[0,90]_{3s}$ and $[90,0]_{3s}$ laminates there is little evidence of this behaviour because the Poisson's ratio of the laminate is close to zero. Conversely in the $[\pm 45]_{3s}$ laminate, $\Delta\varepsilon_x$ decreases whilst $\Delta\varepsilon_y$ increases with loading frequency due to the Poisson's ratio of the laminate.

In all three laminates, the magnitude $\Delta\varepsilon_x$ predicted by the CLT is higher than the measured values, whereas the measured and predicted $\Delta\varepsilon_y$ match more closely. The difference between the measured and predicted strains highlights the uncertainties on the GFRP material properties. Additionally, the LSDIC measured shear strain, $\Delta\varepsilon_{xy}$, was obtained and it was practically zero in all cases, because the x and y axes are axes of principal stress and strain.

It should be noted that a similar exercise was carried out on the CFRP specimens and it was seen that measured and CLT predicted strains showed a good agreement validating the CFRP material properties.

However, the LSDIC measured strains showed a similar reduction in magnitude with respect to the loading frequency as also seen for the GFRP laminates.

The outcome from this section of the paper is that an independent measure of strain is required in any TSA calibration process to account for heat transfer effects, as using the target applied load from the test machine will introduce large uncertainties as loading frequencies increase. Hence, in the following section, the strains obtained from the LSDIC are used to provide a predicted $\Delta T/T_0$ that is compared with the measured $\Delta T/T_0$, with the certainty that the LSDIC and TSA are experiencing exactly the same loading conditions. In the current experimental campaign, it is not necessary to use full-field measurements to obtain the strain, as the field is uniform, so the readings from the strain gauge would be sufficient to monitor the load behaviour. However, the full-field strain measurements allow non-uniform loading to be monitored. Moreover, for typical components, the surface strain field will be non-uniform and, hence, a reading from a single strain gauge will not be sufficient for calibration purposes.

4.3. Comparison of $\Delta T/T_0$ derived from TSA, LSDIC and Strain Gauges

Figure 9 shows examples of $\Delta\varepsilon_x$, $\Delta\varepsilon_y$ and $\Delta T/T_0$ full-field images obtained with LSDIC and TSA for the $[0,90]_{3s}$ GFRP and CFRP specimens at 3.1 Hz loading frequency; in all cases the measurement is practically uniform across the sample surface. Hence, an average across the specimen area was extracted to present the measured and calculated $\Delta T/T_0$ with respect the loading frequency to assess heat transfer and the source of the thermoelastic response.

Figure 10 shows the normalised thermoelastic response for the three GFRP coupons with respect to the loading frequency. The actual measure of the thermoelastic response is shown, alongside the predicted response using the LSDIC measured strains for the three scenarios formulated in section 2. In all cases, the unpainted specimens provide a greater measured $\Delta T/T_0$ than the painted specimens. Moreover, the response from the painted specimens reduces significantly with loading frequency; this is not evident in the unpainted specimens. As the measured paint thickness is 18.32 ± 2.73 μm (see Table 4), the indication is that paint thicknesses greater than 18 μm would cause attenuation of the thermoelastic response. Further analysis on the paint thickness is shown in section 4.4. As the loading frequency increases, the response reduces further

indicating that the thermal diffusion length generated within one cycle is not large enough for the response to diffuse through the paint coating.

Focusing on the thermoelastic response from the unpainted specimen and comparing with the predicted response from the LSDIC, it is clear in all three cases that the actual $\Delta T/T_0$ corresponds most closely with the predicted values for the resin. A further observation is that the response does not vary with loading frequency indicating clearly, as concluded in previous works [6-9], that the thermoelastic response is that of the isolated isotropic resin-rich layer. However, it is the case that the predictions of $\Delta T/T_0$ do not match exactly the measured data. For the $[90,0]_{3s}$ (Figure 10 (b)), the measurements and the predictions are very close, with predictions slightly greater than the measurements. For the other two laminates, the difference between the measurements and the predictions is much greater, with the predictions being less than the measured values. Interestingly, the predicted LSDIC values for the surface ply and the laminate are very close for the $[0,90]_{3s}$ and $[90,0]_{3s}$ specimens, with $\Delta T/T_0$ being $\sim 3.2 \cdot 10^{-4}$. This is because the combination of the stress carried by the ply and the coefficients of thermal expansion of the ply results in a similar value for both lay-ups. Considering the potential systematic errors in the material property values and scatter in the data indicated by the error bars (standard deviation) in Figure 10, it is difficult to make any further conclusions regarding the heat transfer characteristics in the GFRP specimens.

Figure 11 shows the normalised thermoelastic response for the three CFRP coupons with respect to the loading frequency. Figure 11 shows for the $[0,90]_{3s}$ sample the measured $\Delta T/T_0$ decreases and for the $[90,0]_{3s}$ laminate $\Delta T/T_0$ increases when the loading frequency increases, similar to [14]. Therefore, it can be concluded that heat transfer is occurring due to the difference in the stress induced temperature change between the 0° and 90° plies. In the $[0,90]_{3s}$, the stress induced temperature change in the 90° subsurface ply is greater than in the 0° surface ply, hence, at lower frequencies there is heat transfer from the subsurface ply to the surface ply, which at higher frequencies does not occur as the thermal diffusion length reduces. In the $[90,0]_{3s}$, as in the 0° subsurface ply the stress induced temperature change is lower than in the 90° surface ply, heat transfers from the surface ply to the subsurface ply, which is possible at low frequencies, but at higher frequencies, as the thermal diffusion length decreases, heat transfer reduces and the thermoelastic response of the surface ply is larger. Figure 11 shows that for both the cross-ply laminates $\Delta T/T_0$ corresponds to the homogenised global laminate response at low loading frequencies and to the

orthotropic surface ply at high loading frequencies. Regarding the $[\pm 45]_{3s}$ specimen, (Figure 11 (c)), the stress induced temperature change is the same for every ply, so heat transfer cannot occur and $\Delta T/T_0$ is constant over the frequency range, with the predicted values for the laminate and the surface ply being equal.

To sum up, in comparison with the CFRP, the GFRP stress induced temperature change between the 0° and 90° plies is similar, hence there is no opportunity for heat transfer, and $\Delta T/T_0$ is unaffected by the loading frequency. The difference between the thermoelastic response from CFRP and GFRP corresponds with a much thinner resin-rich surface layer for the CFRP (5.10 ± 3.69 μm) in comparison with the GFRP (16.66 ± 9.69 μm), which allows heat transfer to the surface, highlighted by the $[0,90]_{3s}$ and $[90,0]_{3s}$ laminates, as the stress induced temperature change of the 0° and 90° plies is significantly different. Another consideration is the volume fraction of the fibres, in the CFRP this is higher than in the GFRP (0.63 ± 0.03 compared to 0.54 ± 0.06). Additionally, although the epoxy resin has a low thermal conductivity, unlike the glass fibre, carbon fibre is conductive, with the larger fibre volume fraction of the CFRP, more fibres will be in contact across plies aiding heat transfer from ply-to-ply.

4.4. Peel Ply Imprint

To examine the effect of the peel ply imprint on the thermoelastic response, three painted GFRP specimens are studied. The samples were different to those used in section 4.3, but were cut from the same panels. Hence, these specimens were painted with a focus on achieving a thinner layer of paint, as thick paint layers were seen to have a detrimental effect in the previous section. Figure 12 shows the normalised thermoelastic response on the smooth and peel ply sides with respect to the loading frequency of painted GFRP specimens. As the results presented in the previous section showed that the thermoelastic response of the GFRP material is driven by the resin, only the predicted thermoelastic response obtained for the resin-rich surface layer is presented. It is clear from Table 4 that the resin is much thicker on the peel ply side than on the smooth side, making the laminate non-symmetrical. Notwithstanding that the resin layer stiffness is small, it could have an effect on the strains. This was checked against CLT predictions, with the calculated strains for the non-symmetrical laminate being practically identical to the symmetrical laminate, i.e. strain sum, $\Delta(\varepsilon_x + \varepsilon_y)$, $1.264 \cdot 10^{-3}$ versus $1.277 \cdot 10^{-3}$ for $[\pm 45]_{3s}$ laminates. Additionally, as the peel ply

imprint causes aliasing in the DIC, the LSDIC strains were obtained from the smooth side; as no damage was occurring, this is justified as strain compatibility is maintained.

The results in Figure 12 show that the $\Delta T/T_0$ from the peel ply side attenuates severely when the loading frequency increases. This is attributed to the thickness of the paint, which is almost double to that on the smooth side (see Table 4). $\Delta T/T_0$ from the smooth side converges in all cases between 10.1 and 20.1 Hz, indicating adiabatic conditions are prevailing. This result contrasts with the results given in Figure 10, where there is no indication of convergence to a constant value suggesting that the paint is thinner than on the specimens presented in section 4.3. The paint thickness was measured and compared (see Table 4), on the smooth side it was 18.32 ± 2.73 µm for the GFRP specimens in section 4.3 versus 12.94 ± 2.65 µm for the specimens in this section. The paint thickness plays an important role on the thermoelastic response and a layer of $\sim 23.17 \pm 5.32$ µm, as seen on the peel ply side, attenuates the response significantly when the loading frequency increases. The variability of the measured thermoelastic response from specimens with different paint thickness applied highlights the dependency on the operator applying the paint and the care required when applying the paint, and where possible tests should be conducted without paint.

5. Conclusions

A new means of analysing the nature or source of the thermoelastic response has been presented that is based on using a measured strain determined from DIC and strain gauge measurements. The approach allows uncertainties in the loading to be accounted for, particularly those associated with test machine capability to achieve a consistent peak to peak load range at high loading frequencies. The new approach utilises the 'lock-in' processing for TSA based on a least-squares fit to the strains from images obtained at low frame rates derived by the DIC (LSDIC) high resolution strain data. The approach was verified using strain gauges, which confirmed that the LSDIC measured strains corresponded directly to the strains measured with the strain gauges. The combination of TSA and the LSDIC establishes a means of monitoring the strain (DIC) alongside the thermal response (TSA) in a full-field manner, which could be applied to larger structures that contain strain gradients and for the monitoring of damaged composite structures.

The focus of the paper is to determine the source of the normalised thermoelastic response, $\Delta T/T_0$. Both the temperature change and the mean surface temperature are measured quantities extracted from an IR

image series. The measured $\Delta T/T_0$ was compared with predicted values based on the strain measurements, enabling the source of the thermoelastic response to be identified categorically. The accurate derivation $\Delta T/T_0$ from the LSDIC was facilitated by a detailed experimental campaign and literature review, which provided well documented values for two typical material types: a GFRP and a CFRP. Micrographs were used to obtain paint and resin-rich layer thicknesses as well as fibre volume fraction. Study of the material thermal properties with respect to the fibre volume fraction was carried out to verify the thermal properties obtained from the literature. All the required material properties were measured apart from the coefficients of thermal expansion and specific heat, which were taken from the literature. There is a high degree of confidence in the coefficients of thermal expansion as the ratio $K_2/K_1 = \alpha_2/\alpha_1$ was confirmed experimentally for both the CFRP and GFRP. The specific heat for the GFRP was calculated using rule of mixtures. A sensitivity study was carried out on variations in specific heat for different values given in the literature which had no significant effect on the results. Different laminate stacking sequences were studied, i.e. two cross-ply ($[0,90]_{3s}$, $[90,0]_{3s}$) and a shear dominated laminate ($[\pm 45]_{3s}$). $\Delta T/T_0$ was calculated from the LSDIC measured strains using three different scenarios (considering the resin-rich surface layer, orthotropic surface ply and global laminate), and compared with the $\Delta T/T_0$ obtained directly from the IR images using TSA.

It was shown that with an accurate knowledge of material properties, the measurement of the strain using LSDIC enables an independent 'measure' of the thermoelastic response to be calculated without any influence of heat transfer. Comparing this with the measured $\Delta T/T_0$ values demonstrated that in the GFRP the source of the thermoelastic response was the resin-rich surface layer. In the GFRP laminates, the stress induced temperature change ply-by-ply is similar because of the combination of coefficients of thermal expansion and material stiffness. Hence, even if the resin-rich surface layer was removed, no heat transfer could take place and, for any symmetrical laminate stacking sequence with these material properties, ΔT would occur adiabatically. The outcome results in a very important conclusion that for most glass fibre based composite laminates (including those with resins other than epoxy that dive a similar ratio of coefficients of thermal expansion and stiffness), the thermoelastic relationship given in equation (1) is always valid as ΔT will always occur adiabatically, as ply-by-ply the material is in thermal equilibrium. Moreover, when the resin-rich surface layer thickness is greater than 16.66 ± 9.69 μm, the response follows equation (4), which is a combination of orthotropic elastic properties and isotropic thermal

properties. Further work is required to establish the minimum thickness of the resin-rich surface layer where equation (4) can be applied. However, controlling the thickness of the resin and maintaining a uniform surface represents a challenge in manufacturing as this is determined by resin bleed out during curing.

For the CFRP, the response was heavily influence by heat transfer, as the ply-by-ply stress induced temperature change for the $[90,0]_{3s}$ and $[0,90]_{3s}$ is markedly different, and because the fibre volume fraction is higher and the resin-rich surface layer much thinner than for the GFRP laminates. An attenuation in response with frequency was evident for the $[0,90]_{3s}$ laminate, as the subsurface ply was transferring heat to the surface ply. Conversely for the $[90,0]_{3s}$ laminate, the response was amplified with frequency as the surface ply was transferring heat to the subsurface ply. At approximately 30 Hz the response tended to that predicted for the orthotropic surface ply, whilst at low loading frequencies the response tended to that predicted for the global laminate. In the $[\pm 45]_{3s}$ lay-up for CFRP, the ply-by-ply stress induced temperature change is identical and hence this laminate displayed an adiabatic response regardless of loading frequency. As with the GFRP, some important conclusions can be drawn from this work. Namely, for the given fibre volume fraction and resin-rich surface layer thickness, equation (1) is only valid for frequencies of around 30 Hz. However, this result cannot be considered universal for carbon fibre laminated composites. The ability to transfer heat is not just driven by the temperature gradient between the plies, but also the thermal conductivity of the carbon fibre itself, in turn aspects such as ply thickness will also have an effect. The IM7/8552 material used here has a ply thickness of 0.131 mm and is considered a 'thin ply' material. Clearly, future work could consider thicker plies to determine their effect on heat transfer. The high fibre volume fraction of the CFRP material also plays a role and this means greater contact between fibres and better paths for conduction. A further conclusion that can be drawn is that the resin-rich surface layer is about 5.10 ± 3.69 μm for this material, and hence indicates a possible minimum resin-rich surface layer thickness for equation (4) to be valid, particularly, as the stress induced temperature change in the $[0,90]_{3s}$ CFRP is much less than of the GFRP.

The work described in the paper has also exposed a further and little considered matter relating to the effect of the paint coating on the response. The paint thickness plays an important role by attenuating the TSA response at high loading frequencies if the paint thickness is high i.e. ~23 μm. The peel ply imprint on the surface of composite components often means it is not necessary to paint the material as this generally has

a greater emissivity. This was not explored in the paper and is clearly an avenue for more research. However, it was shown that painting over the peel ply imprint significantly attenuated the thermoelastic response. A major conclusion is the paint application, which is operator dependent, is of significant importance. Thus, if paint is necessary, the paint layer thickness should be as thin as possible and uniform, otherwise the measured thermoelastic response will vary over the region of interest making any quantitative comparisons very difficult.

The indications are that GFRP is an easier material to deal with in terms of TSA, but in general these materials are not as well characterised and are usually manufactured by a process that result in lower quality material with variations in fibre volume fraction over the laminate. In contrast, CFRP lends itself to more consistent manufacturing with a focus on high quality (aerospace) laminates with well characterised properties. The overarching conclusion is that accurate interpretation of the thermoelastic response from laminated orthotropic composites is possible. However, it is dependent on several competing factors, and it is recommended that a careful experimental calibration procedure is carried out, as described in the paper to determine the source of the thermoelastic response, prior to embarking on an experimental campaign on actual components.

Figures

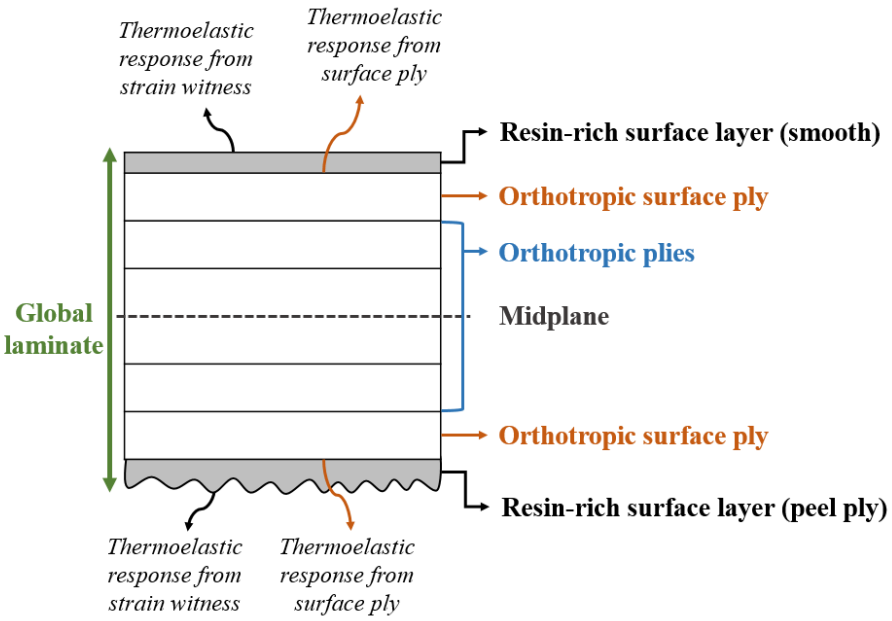

Figure 1 Cross-section of multi-directional symmetric laminate showing nomenclature

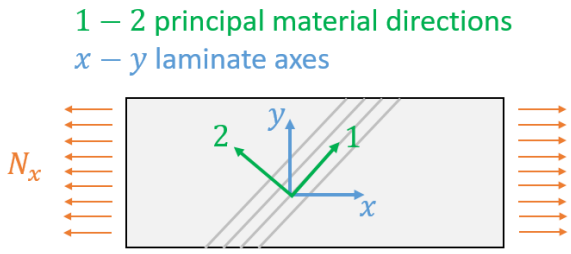

Figure 2 Coordinate systems for coupon under uniaxial tension load

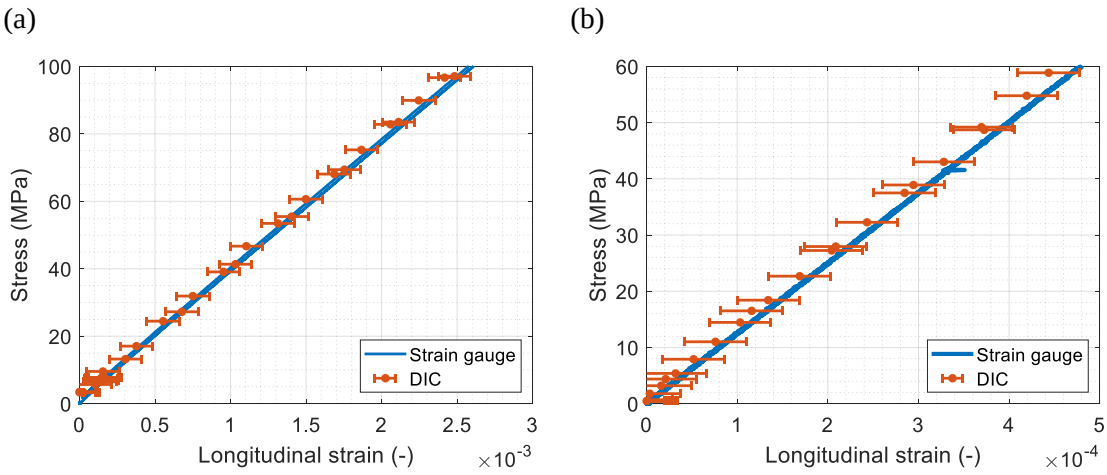

Figure 3 0UD stress vs strain (a) GFRP and (b) CFRP

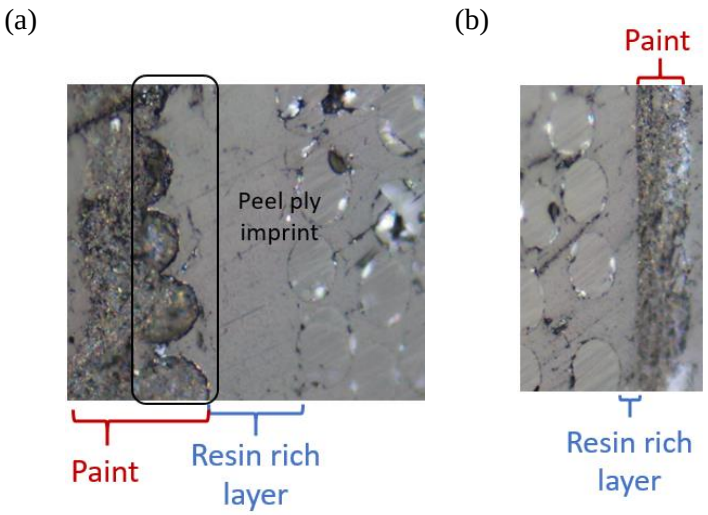

Figure 4 Micrographs from GFRP specimens (a) peel ply side and (b) smooth side

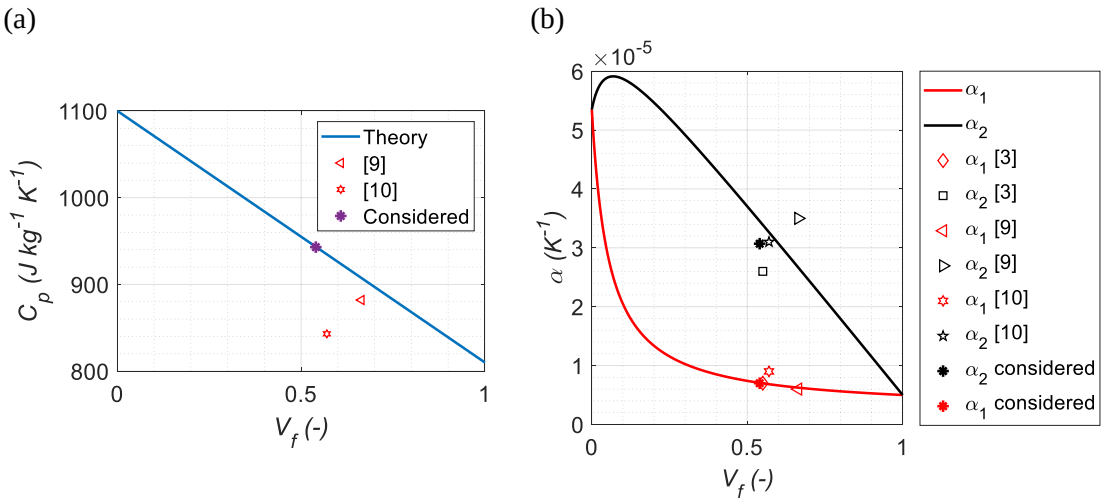

Figure 5 (a) C_p plotted against V_f for GFRP using the rule of mixtures, (b) α_1 and α_2 plotted against V_f for GFRP using the Schapery's equations

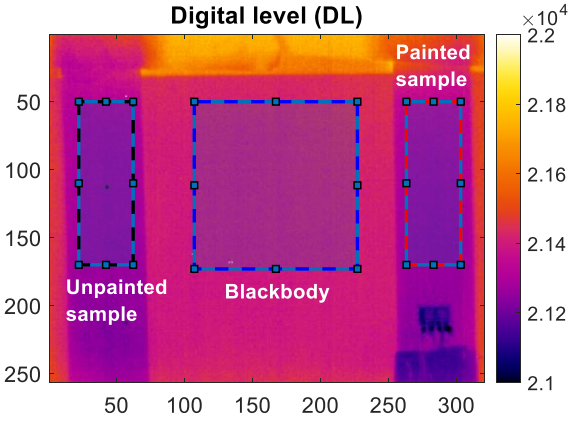

Figure 6 IR image of the comparative experiment to obtain emissivity in DL: GFRP specimens without paint (left) and with paint (right) applied to the surface

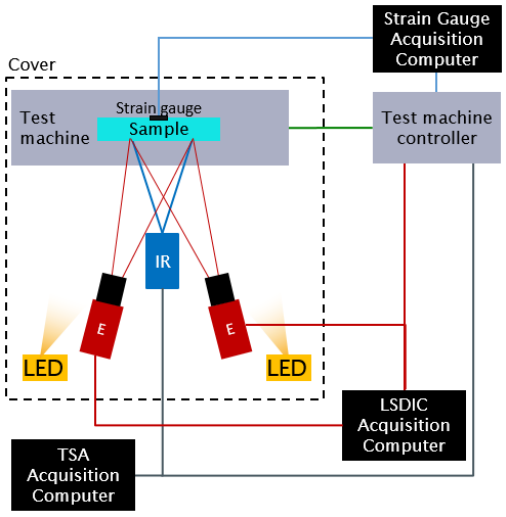

Figure 7 Experimental setup

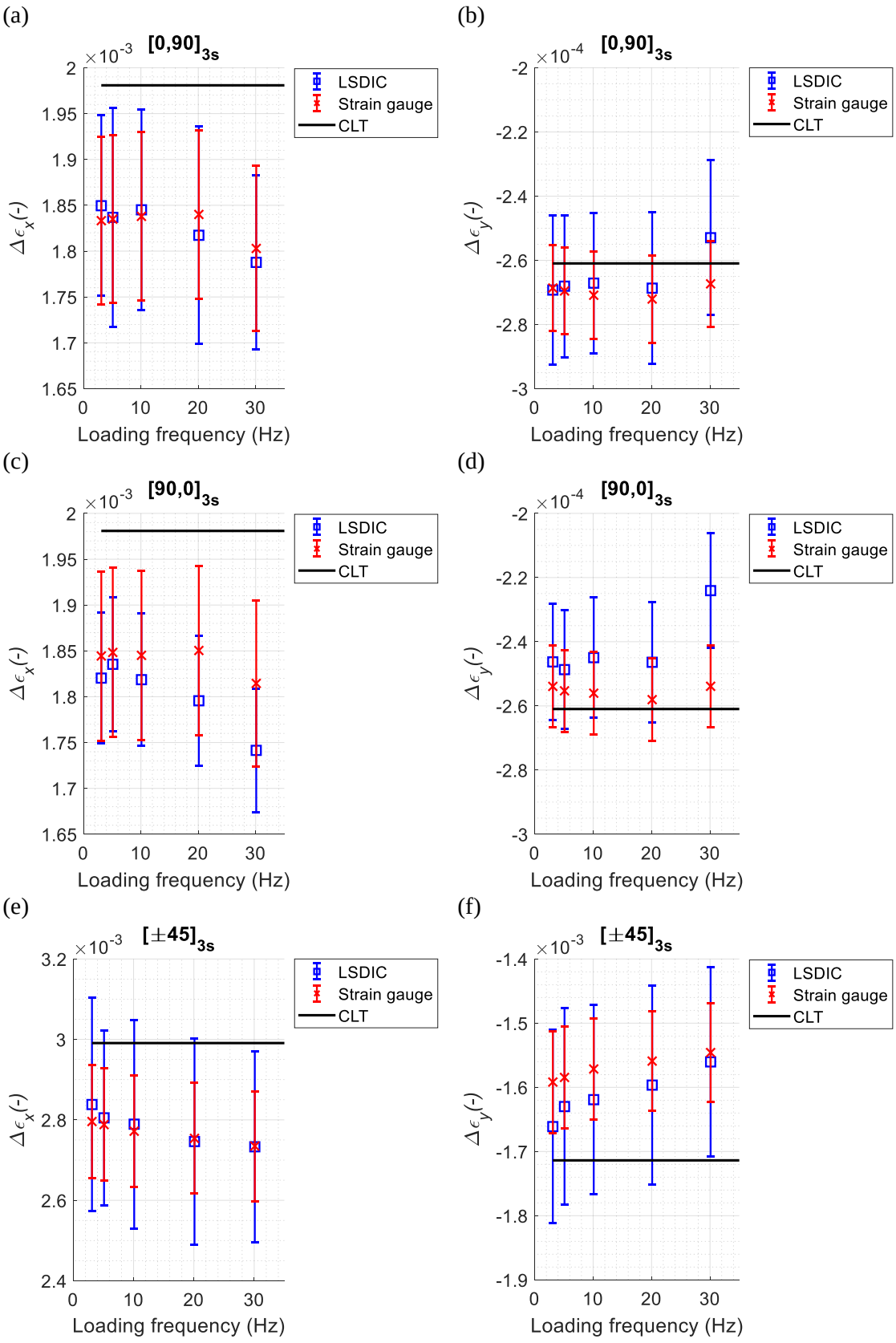

Figure 8 GFRP strain comparison LSDIC, strain gauge and CLT being (a) and (b) the $\Delta\varepsilon_x$ and $\Delta\varepsilon_y$ of the $[0,90]_{3s}$ sample; (c) and (d) the $\Delta\varepsilon_x$ and $\Delta\varepsilon_y$ of the $[90,0]_{3s}$ sample; and (e) and (f) the $\Delta\varepsilon_x$ and $\Delta\varepsilon_y$ of the $[\pm45]_{3s}$ sample

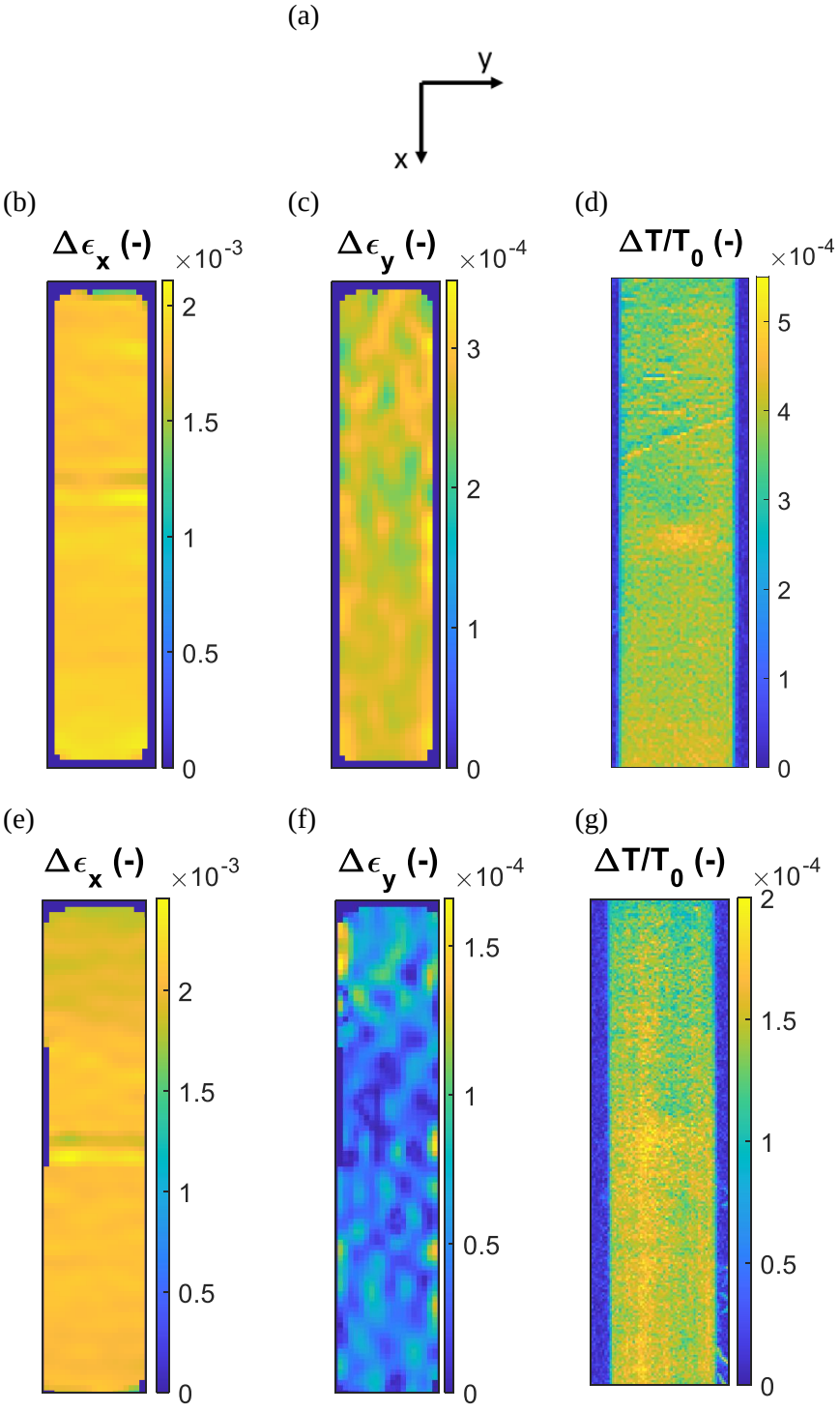

Figure 9 Example of full-field images for the $[0,90]_{3s}$ sample at 3.1 Hz loading frequency. (a) coordinate system, (b)-(d) GFRP and (e)-(g) CFRP results

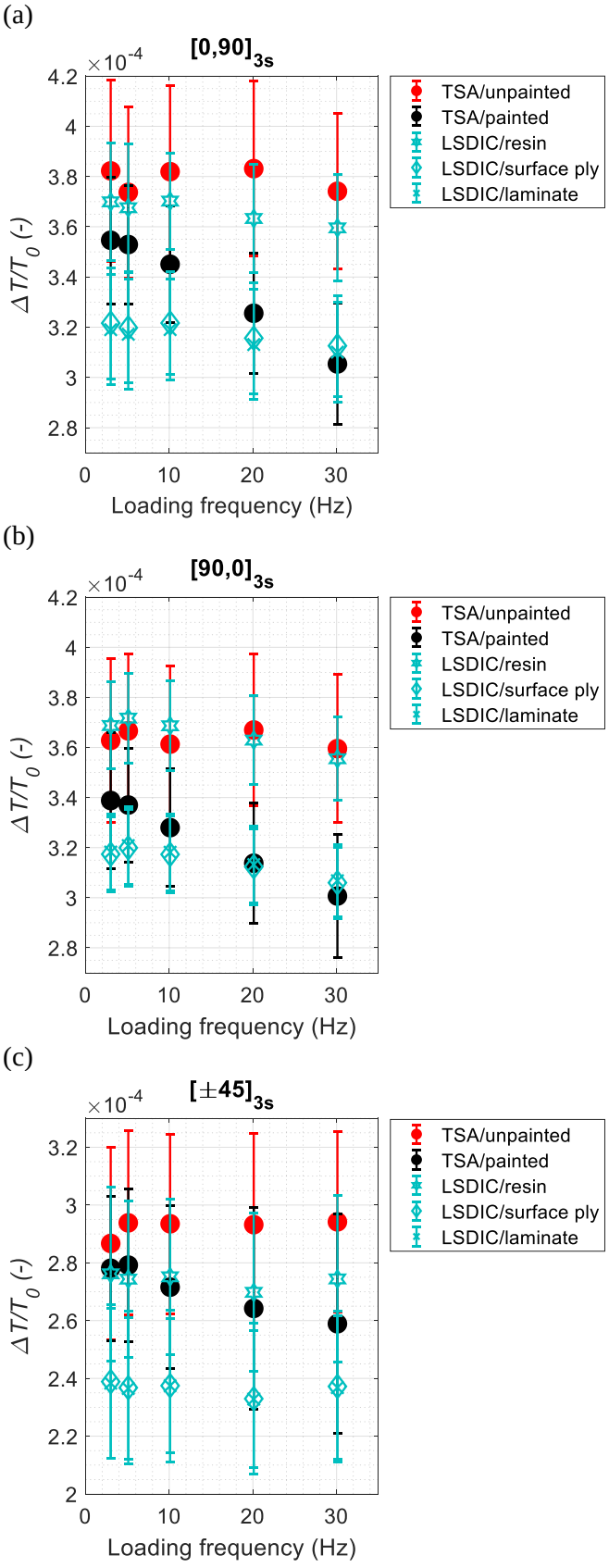

Figure 10 Normalised thermoelastic response $\Delta T/T_0$ vs loading frequency of (a) $[0,90]_{3s}$, (b) $[90,0]_{3s}$ and (c) $[\pm 45]_{3s}$ GFRP specimens

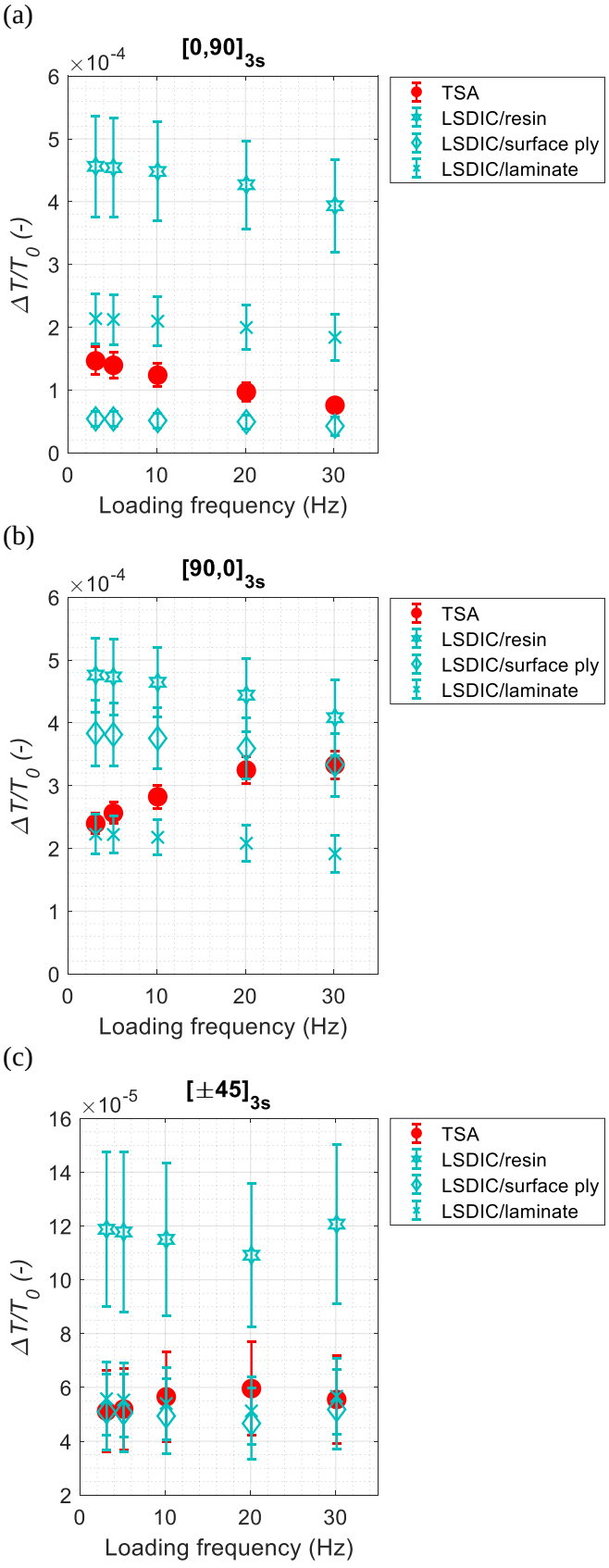

Figure 11 Normalised thermoelastic response $\Delta T/T_0$ vs loading frequency of (a) $[0,90]_{3s}$, (b) $[90,0]_{3s}$ and (c) $[\pm 45]_{3s}$ CFRP specimens

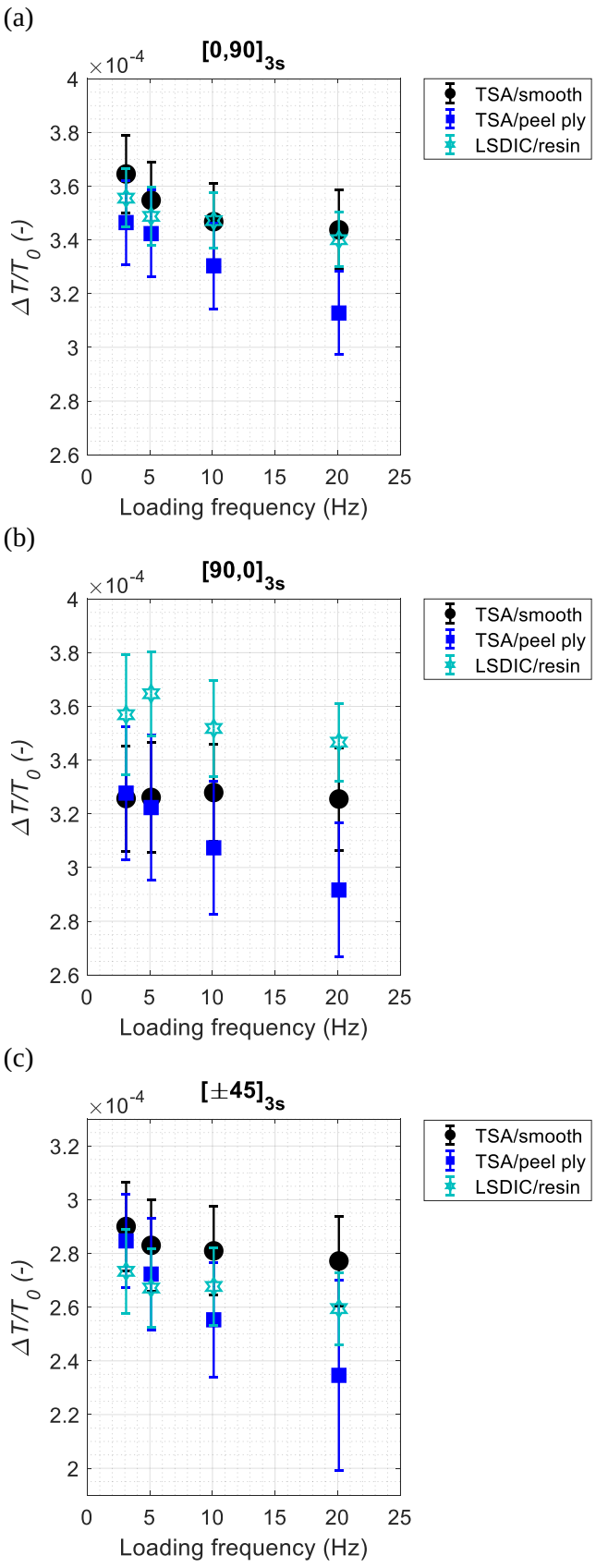

Figure 12 Normalised thermoelastic response $\Delta T/T_0$ vs loading frequency of painted (a) $[0,90]_{3s}$, (b) $[90,0]_{3s}$ and (c) $[\pm 45]_{3s}$ GFRP specimens comparing smooth and peel ply surface finish

Tables

Table 1 Specimen dimensions

Specimen type	GFRP			CFRP		
	Length (mm)	Width (mm)	Thickness (mm)	Length (mm)	Width (mm)	Thickness (mm)
0 UD: $[0]_{10}$	270	15	2.36	220	25*	1.31
90 UD: $[90]_{10}$	235	25	2.36	175	25	1.31
$[0, 90]_{3s}$	220	25	2.76	220	25	1.527
$[90, 0]_{3s}$	220	25	2.76	220	25	1.527
$[\pm 45]_{3s}$	250	25	2.76	220	25	1.527

* This does not conform the recommended width in the standard because a wider sample was required for the TSA work on the UD carbon to give more measurement points

Table 2 Material properties

Property	GFRP			CFRP		
	DIC	Strain gauge	Average	DIC	Strain gauge	Average
E_1 (GPa)	38.87 $\pm$ 0.09	37.32 $\pm$ 0.07	38.10 $\pm$ 0.83	150.75 $\pm$ 0.50	146.86 $\pm$ 0.02	148.80 $\pm$ 2.27
ν_{12}	0.311 $\pm$ 0.02	0.272 $\pm$ 0.001	0.291 $\pm$ 0.021	0.35 $\pm$ 0.01	0.34 $\pm$ 0.01	0.34 $\pm$ 0.01
E_2 (GPa)	10.74 $\pm$ 0.02	11.43 $\pm$ 0.10	11.08 $\pm$ 0.38	9.11 $\pm$ 0.04	9.27 $\pm$ 0.03	9.19 $\pm$ 0.10
G_{12} (GPa)	3.87 $\pm$ 0.06	3.86 $\pm$ 0.18	3.86 $\pm$ 0.13	5.12 $\pm$ 0.15	5.01 $\pm$ 0.01	5.06 $\pm$ 0.07
ρ (kg/m^3)	-	-	1861.6 $\pm$ 3.4	-	-	1556.75 $\pm$ 72.5

Table 3 Epoxy resin elastic properties

Resin property	Value
ρ_r (kg/m^3)	1153
E_r (GPa)	3.8
ν_r	0.35
G_r (GPa)	1.41

Table 4 Volume fraction and resin-rich layer thickness

			GFRP	CFRP
Fibre diameter (μm)			13.59 ± 0.92	5.0 ± 0.3
Micrograph area (μm²)			23,400	5,570
V_f			0.54 ± 0.06	0.63 ± 0.03
Resin-rich layer thickness (μm)	**Smooth side**		16.66 ± 9.69	5.10 ± 3.69
	Peel ply side		28.62 ± 8.47	-
Paint thickness (μm)	**Smooth side**	**Used in Section 4.3**	18.32 ± 2.73	-
		Used in Section 4.4	12.94 ± 2.65	-
	Peel ply side - Used in Section 4.4		23.17 ± 5.32	-

Table 5 Glass fibre and resin thermal properties

	$C_p\ (\mathrm{J\,kg^{-1}K^{-1}})$	$\alpha\ (\cdot 10^{-6}\ \mathrm{K^{-1}})$
E-glass fibre	810 [33]	5 [3]
Resin	1100 [34]	53.5 (mean value from [3])

Table 6 Coefficients of thermal expansion for IM7/8552 from literature

	Reference [23]	**Reference [24]**
V_f	0.591	0.577
$\alpha_1\ (\cdot 10^{-6}\ \mathrm{K^{-1}})$	-0.5	-0.1
$\alpha_2\ (\cdot 10^{-6}\ \mathrm{K^{-1}})$	25.8	31

Table 7 Ratio of coefficients of thermal expansion

Properties	**GFRP**	**CFRP**
$\alpha_1\ (\cdot 10^{-6}\ \mathrm{K^{-1}})$*	7	-0.3
$\alpha_2\ (\cdot 10^{-6}\ \mathrm{K^{-1}})$*	30.7	28.4
α_2/α_1	$\mathbf{4.4}$	$\mathbf{94.7}$
$K_1\ (\mathrm{MPa^{-1}})$**	4.4 ± 0.4	0.17 ± 0.06
$K_2\ (\mathrm{MPa^{-1}})$**	18.7 ± 1.8	16.0 ± 1.0
K_2/K_1	$\mathbf{4.3 \pm 0.6}$	$\mathbf{94.1 \pm 0.5}$

* obtained from the literature; ** determined experimentally

Table 8 Digital level and emissivity for each element

	DL	e
Blackbody	21407.21 ± 20.52	0.96 ± 0.02
GFRP epoxy (smooth)	21287.09 ± 26.48	0.95 ± 0.02
Paint on GFRP epoxy (smooth)	21285.94 ± 29.74	0.95 ± 0.02

Table 9 Applied load and stress and FPF for the different stacking sequences and materials

	$[0, 90]_{3s}$ and $[90, 0]_{3s}$			$[\pm 45]_{3s}$		
	Applied load (kN)	**Applied stress (MPa)**	**FPF stress (MPa)**	**Applied load (kN)**	**Applied stress (MPa)**	**FPF stress (MPa)**
GFRP	2 ± 1.67	53	115.63	2 ± 1.24	47	78.07
CFRP	4 ± 3.4	194	542	1 ± 0.9	50	174

Acknowledgements

This work was supported by the Engineering and Physical Sciences Research Council [grant number EP/P006701/1], as part of the EPSRC Future Composites Manufacturing Research Hub. The experimental work described in the paper was conducted in the Testing and Structures Research Laboratory (TSRL) at the University of Southampton. The authors acknowledge the support received from Dr Andy Robinson, the TSRL Principal Experimental Officer. The authors would also like to thank Dr Karthik 'Ram' Ramakrishnan for manufacturing of the CFRP panels at the University of Bristol.

Appendix

Table 10 Summary of the properties used in the calculations for orthotropic GFRP and CFRP materials

Property	**GFRP**	**CFRP**
E_1 (GPa)	38.10 ± 0.83	148.80 ± 2.27
ν_{12}	0.291 ± 0.021	0.34 ± 0.01
E_2 (GPa)	11.08 ± 0.38	9.19 ± 0.10
G_{12} (GPa)	3.86 ± 0.13	5.06 ± 0.07
ρ (kg/m^3)	1861.6 ± 3.4	1556.75 ± 72.5
C_p (J kg^{-1}K^{-1})	940	857
α_1 ($\cdot 10^{-6}$ K^{-1})	7	-0.3
α_2 ($\cdot 10^{-6}$ K^{-1})	30.7	28.4

Table 11 Resin properties used

Property	**Resin**
E_r (GPa)	3.8
ν_r	0.35
G_r (GPa)	1.41
ρ_r (kg/m^3)	1153
C_{p_r} (J kg^{-1}K^{-1})	1100
α_r ($\cdot 10^{-6}$ K^{-1})	53.5

Table 12 DIC performance evaluation

Experiments	**Mechanical properties GFRP**		**LSDIC GFRP**		**Mechanical properties and LSDIC CFRP**	
Technique used	**3D digital image correlation**					
	Camera 1	**Camera 2**	**Camera 1**	**Camera 2**	**Camera 1**	**Camera 2**
Sensor and digitization	2448 x 2050, 12-bit					
Camera noise (% of range)	0.78 %	0.74 %	0.66 %	0.65 %	1.57 %	1.78 %
Lens and imaging distance	50 mm F-mount, 1.1 m				50 mm F-mount, 1 m	
Total number of images	2 (1.5 Hz)					
Pixel to mm conversion	1 pixel = 0.070 mm		1 pixel = 0.067 mm		1 pixel = 0.059 mm	
ROI (mm)	150 x 25 mm		140 x 25 mm		113 x 25 mm	
Subset, step	61, 20					
Interpolation, shape functions, correlation criterion	Bicubic (6^{th} order spline), affine, ZNSSD					
Pre-smoothing	None					
Displacement resolution	$1.30 \cdot 10^{-3}$ mm		$2.66 \cdot 10^{-3}$ mm		$1.05 \cdot 10^{-3}$ mm	
Strain						
Smoothing technique	Local polynomial - affine least-squares fit					
Strain window	3 data points					
VSG	102 pixels					
Resolution	0.0108 %		0.0148%		0.0028 %	

References

[1] J. M. Dulieu-Barton, "Thermoelastic Stress Analysis," in *Optical methods for solid mechanics*, P. Rastogi and E. Hack Eds. Weinheim: Wiley-VCH, 2012, ch. 8.

[2] P. Stanley and W. K. Chan, "The application of thermoelastic stress analysis techniques to composite materials", *The Journal of Strain Analysis for Engineering Design*, Article vol. 23, no. 3, pp. 137-143, 1988, doi: https://doi.org/10.1243%2F03093247V233137.

[3] I. M. Daniel and O. Ishai, *Engineering Mechanics of Composite Materials*, Second Edition ed. 2006.

[4] A. K. Wong, "A Non-Adiabatic Thermoelastic Theory for Composite Laminates", *Journal of Physics and Chemistry of Solids*, vol. 52, no. 3, pp. 483-494, 1991, doi: https://doi.org/10.1016/0022-3697(91)90180-8.

[5] D. Zhang, N. F. Enke, and B. I. Sandor, "Thermographic Stress Analysis of Composite Materials", *Experimental Mechanics*, vol. 30, no. 1, pp. 68-73, 1990, doi: https://doi.org/10.1007/BF02322705.

[6] P. R. Cunningham, J. M. Dulieu-Barton, A. G. Dutton, and R. A. Shenoi, "The effect of ply lay-up upon the thermoelastic response of laminated composites", *Key Engineering Materials*, Conference Paper vol. 221-222, pp. 325-336, 2002, doi: https://doi.org/10.4028/www.scientific.net/KEM.221-222.325.

[7] G. Pitarresi, M. S. Found, and E. A. Patterson, "An investigation of the influence of macroscopic heterogeneity on the thermoelastic response of fibre reinforced plastics", *Composites Science and Technology*, vol. 65, no. 2, pp. 269-280, 2005, doi: https://doi.org/10.1016/j.compscitech.2004.07.008.

[8] G. Pitarresi, A. Conti, and U. Galietti, "Investigation on the Influence of the Surface Resin Rich Layer on the Thermoelastic Signal from Different Composite Laminate Lay-Ups", *Applied Mechanics and Materials*, vol. 3-4, pp. 167-172, 2006, doi: https://doi.org/10.4028/www.scientific.net/AMM.3-4.167.

[9] T. R. Emery, J. M. Dulieu-Barton, J. S. Earl, and P. R. Cunningham, "A generalised approach to the calibration of orthotropic materials for thermoelastic stress analysis", *Composites Science and Technology*, vol. 68, pp. 743-752, 2008, doi: https://doi.org/10.1016/j.compscitech.2007.09.002.

[10] S. Sambasivam, S. Quinn, and J. M. Dulieu-Barton, "Identification of the source of the thermoelastic response from orthotropic laminated composites", in *17th International Conference on Composite Materials*, Edinburgh, United Kingdom, 2009: IOM Communications Ltd.

[11] R. K. Fruehmann, J. M. Dulieu-Barton, and S. Quinn, "On the thermoelastic response of woven composite materials", *The Journal of Strain Analysis for Engineering Design*, vol. 43, no. 6, pp. 435-450, 2008, doi: https://doi.org/10.1243%2F03093247JSA381.

[12] R. K. Frühmann, S. Sambasivam, J. M. Dulieu-Barton, and S. Quinn, "Material Properties for Quantitative Thermoelastic Stress Analysis of Composite Structures", *Applied Mechanics and*

Materials, vol. 13-14, pp. 99-104, 2008, doi: https://doi.org/10.4028/www.scientific.net/AMM.13-14.99.

[13] S. Quinn and J. M. Dulieu-Barton, "Identification of the sources of non-adiabatic behaviour for practical thermoelastic stress analysis", *Journal of Strain Analysis*, Article vol. 37, pp. 59-72, 2002, doi: https://doi.org/10.1243/0309324021514835.

[14] D. A. Crump and J. M. Dulieu-Barton, "Assessment of non-adiabatic behaviour in thermoelastic stress analysis of composite sandwich panels", *Experimental Mechanics*, vol. 52, pp. 829-842, 2012, doi: https://doi.org/10.1007/s11340-012-9601-9.

[15] F. Hild and S. Roux, "Digital Image Correlation," in *Optical methods for solid mechanics*, P. Rastogi and E. Hack Eds. Weinheim: Wiley-VCH, 2012, ch. 5.

[16] R. K. Fruehmann, J. M. Dulieu-Barton, S. Quinn, and J. P. Tyler, "The use of a lock-in amplifier to apply digital image correlation to cyclically loaded components", *Optics and Lasers in Engineering*, Article vol. 68, pp. 149-159, 2015, doi: https://doi.org/10.1016/j.optlaseng.2014.12.021.

[17] *Toughened Epoxy Prepreg System RP-528*, Dorset, England, UK, 2016.

[18] Hexcel. Product Data Sheet HexPly 8552 [Online] Available: https://www.hexcel.com/Resources/DataSheets/Prepreg

[19] Hexcel. Product Data Sheet HexTow IM7 [Online] Available: https://www.hexcel.com/Resources/DataSheets/Carbon-Fiber

[20] R. Ponginan. "ESAComp Theoretical Background - Analyses - Part 3 - Laminates". https://altairuniversity.com/learning-library/esacomp-theoretical-background-analyses-part-3-laminates/ (accessed 2020).

[21] J. Thomason, L. Yang, and F. Gentles, "Characterisation of the Anisotropic Thermoelastic Properties of Natural Fibres for Composite Reinforcement", *Fibers*, vol. 5, no. 4, 2017, doi: https://doi.org/10.3390/fib5040036.

[22] M. T. Saad, S. G. Miller, and T. Marunda, "Thermal Characterisation of IM7/8552-1 Carbon-Epoxy Composites", in *ASME 2014 International Mechanical Engineering Congress and Exposition (IMECE2014)*, Montreal, Quebec, Canada, 2014, doi: https://doi.org/10.1115/IMECE2014-40030.

[23] P. P. Camanho, P. Maimí, and C. G. Dávila, "Prediction of size effects in notched laminates using continuum damage mechanics", *Composites Science and Technology*, vol. 67, no. 13, pp. 2715-2727, 2007, doi: https://doi.org/10.1016/j.compscitech.2007.02.005.

[24] J. P. Stacey, M. O'Donnell, and M. Schenk, "Thermal Prestress in Composite Compliant Shell Mechanisms", in *ASME 2018 International Design Engineering Technical Conferences & Computers and Information in Engineering Conference*, Quebec, Canada, 2018, doi: https://doi.org/10.1115/DETC2018-85826.

[25] Everest Intersicence Inc. "Everest Interscience Emissivity of Total Radiation for Various Metals". http://everestinterscience.com/info/emissivitytable.htm (accessed 2020).

[26] T. Laux, K. W. Gan, J. M. Dulieu-Barton, and O. T. Thomsen, "A simple nonlinear constitutive model based on non-associative plasticity for UD composites: Development and calibration using a Modified Arcan Fixture", *International Journal of Solids and Structures*, vol. 162, pp. 135-147, 2019, doi: https://doi.org/10.1016/j.ijsolstr.2018.12.004.

[27] P. P. Camanho and M. Lambert, "A design methodology for mechanically fastened joints in laminated composite materials", *Composites Science and Technology*, vol. 66, pp. 3004-3020, 2006, doi: https://doi.org/10.1016/j.compscitech.2006.02.017.

[28] *Altair ESAComp*. [Online]. Available: https://altairhyperworks.com/product/esacomp

[29] iDICs, E. M. C. Jones, and M. A. Iadicola, "A good practices guide for digital image correlation", 2018, doi: https://doi.org/10.32720/idics/gpg.ed1/print.format.

[30] J. Q. Zhang, Z. Xinmin, H. Xiao, and S. Jinwei, "Sinewave Fit Algorithm Based on Total Least-Squares Method with Application to ADC Effective Bits Measurement", *IEEE Transactions on Intrumentation and Measurement*, vol. 46, no. 4, pp. 1026 - 1030, 1997, doi: https://doi.org/10.1109/19.650821.

[31] R. K. Fruehmann, D. A. Crump, and J. M. Dulieu-Barton, "Characterization of an infrared detector for high frame rate thermography", *Measurement Science and Technology*, vol. 24, no. 10, p. 105403, 2013, doi: https://doi.org/10.1088/0957-0233/24/10/105403.

[32] J. E. Thatcher, D. A. Crump, C. Devivier, P. B. S. Bailey, and J. M. Dulieu-Barton, "Low cost infrared thermography for automated crack monitoring in fatigue testing", *Optics and Lasers in Engineering*, vol. 126, 2020, doi: https://doi.org/10.1016/j.optlaseng.2019.105914.

[33] MatWeb. E-Glass Fiber, Generic [Online] Available: http://www.matweb.com/search/DataSheet.aspx?MatGUID=d9c18047c49147a2a7c0b0bb1743e812&ckck=1

[34] Substances & Technologies. "Thermoset Epoxy (EP)". http://www.substech.com/dokuwiki/doku.php?id=thermoset_epoxy_ep (accessed 2020).